第57回流体力学講演会/
第43回航空宇宙数値シミュレーション技術シンポジウム
2025年7月2日～4日
タワーホール船堀（東京）

JSASS-2025-2090

3A09　対称的な2次元正方格子パターンインジェクタのRDEのデザインと実験

○ビクトリア・ジョセフ（名古屋大学）、笠原次郎（名古屋大学）、松岡健（名古屋大学），
伊東山登（名古屋大学）、安井正明（名古屋大学）、井出雄一郎（名古屋大学）、
松尾亜紀子（慶應義塾大学）、船木 一幸（国立研究開発法人宇宙航空研究開発機構宇宙科学研究所）
東野和幸(NETS Co. Ltd.)

Design and Experiments of a Symmetric Two-Dimensional Square Lattice Pattern Injector and RDE

Victoria Joseph (Nagoya University), Jiro Kasahara (Nagoya University), Ken Matsuoka (Nagoya University),
Noboru Itouyama (Nagoya University), Masaaki Yasui (Nagoya University), Yuichiro Ide (Nagoya University),
Akiko Matsuo (Keio University), Ikkoh Funaki (JAXA Institute of Space and Astronautical Science,
Kazuyuki Higashino (NETS Co. Ltd.)

Key Words : Wave Motion. Shock Wave. Propulsion.

Abstract

An injector with a symmetric, two-dimensional, square lattice pattern was designed. Tested with a rotating detonation engine (RDE) with a square combustion chamber, tests with gaseous ethylene and gaseous oxygen used total mass flowrates between 30 g/s to 38 g/s and equivalence ratios between 1 to 1.6. The detonation reached 98% of the Chapman-Jouget theoretical wave velocity. The decomposed wave motion showed the horizontal wave velocity was 10% higher than the vertical velocity. This design may therefore increase engine efficiency.

1. Introduction

A rotating detonation engine (RDE) is a more thermodynamically efficient, smaller, and simpler engine than current gas turbine engines [1]. It has a detonation combustion wave propagating in the combustion chamber instead of a regular deflagration combustion wave. Therefore, RDEs are one option for future combustion engines in the aerospace industry [2]. The injector component is a critical part of an RDE because it impacts reactant mixing, wave propagation and stability, and RDE efficiency and propulsive performance [3-7].

RDEs a generally designed in a circular shape (annular or hollow), however, the impact other geometries are still unclear. Thus far, there are limited experimental studies about the effect of different injector geometries than circular injector patterns, and linear channels [7-11]. In this study, an injector component that injected fuel and oxidizer across the entire combustor inlet cross-sectional area was designed and tested.

2. Injector Geometry

The injector geometry is a critical feature of RDE design. Some requirements and discussion about how the final injector design was chosen follows next.

2.1 Requirements

The geometry necessary for a bi-propellant injector component was investigated. In determining the ideal geometry for the study, some restrictions were applied: 1:only basic shapes could be used (a triangle or a square only – a circular injector patterns is generally used in RDE injector design); 2: the resulting pattern from repeating the basic shape had to be symmetric across the entire cross-sectional area – doing so would reduce changes or trends exhibited in a scaled up design; and 3: creating a mixing pattern where the mixing point lattice is interconnected between all injectors.

2.2 The Symmetric Square Lattice Injector Pattern

When considering the above factors, using a repeated square shape produced an acceptable injector pattern. Figure 1 shows the square lattice pattern obtained from using a square shape to design the injector. Placing the oxidizer holes (blue) directly next to the fuel holes (orange) and vice-versa, the internal basic square shape is seen. This pattern can be expanded to produce the RDE injector layout shown in Figure 2. Figure 2 shows how one set of oxidizer holes is equidistant from the

surrounding sets of oxidizer holes in all directions. At the same time, a set of oxidizer holes is also equidistant from each surrounding set of fuel holes in all directions as well. It is this feature that could not be obtained when using a triangle as the basic repeated shape. As such, the injector pattern obtained by repeated the square basic shape resulted in a symmetric, 2-dimensional, square lattice injector pattern that met the design restrictions. The symmetric, square lattice pattern was extended to use it with the square combustion chamber, and created the simple, repeated, symmetric injector pattern in Figure 2.

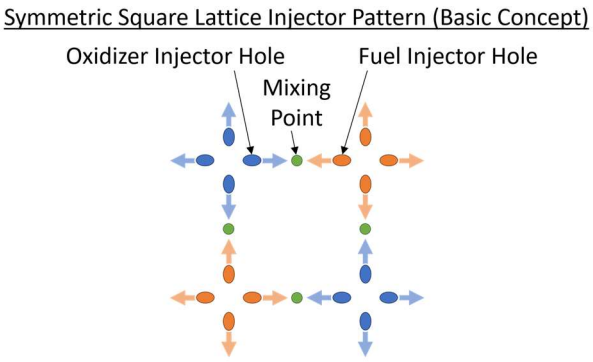

Figure 1: Basic Concept for the Symmetric Square Lattice Injector Pattern

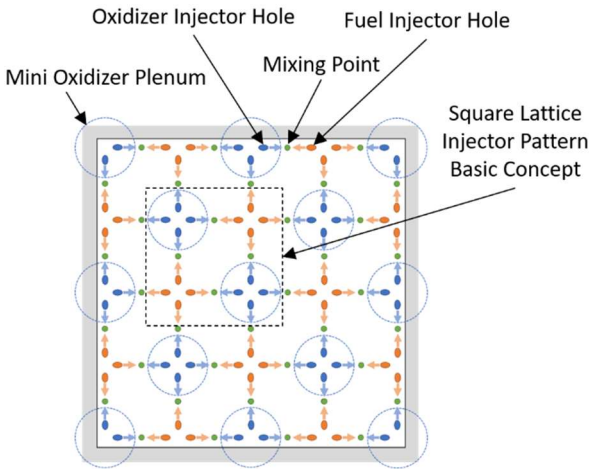

Figure 2: Symmetric Square Lattice Injector Pattern Extended for use with a Square Combustion Chamber

3. RDE Design

The engine consists of the following components: the oxidizer plenum, the dual plenum, and the combustion chamber. The dual plenum component was critical and its unique design was necessary to create the injection flow seen in Figure 2. In general, RDE plenums are not designed in this way and instead have a single cylindrical or annular design, and even recently, a conical RDE [12]. The overall RDE structure is shown in Figure 3. It shows the oxidizer plenum, the first blue component; the dual plenum, containing the orange fuel plenum and blue mini oxidizer plenums (discussed in more detail below); and the white (internally) square combustion chamber. The injector patten is colored in to identify its position relative to the RDE. Figure 4 shows basic engine dimensions and pressure sensor locations. Figure 5 shows a photo of the engine set up and photos of the components looking downstream (D/S) into the engine (to the left of the indicator) and looking upstream (U/S) into the engine (to the right of the indicator).

The dual plenum is a key component to engine design. Its external features are pictured in Figure 5. The dual plenum is a hollow cylindrical piece with smaller cylindrical passages (seen in Figure 5 D/S) within the main volume. The main volume of the dual plenum is the fuel plenum section. The internal cylindrical passages connect the oxidizer plenum above to the injector surface below. In Figure 5, the upstream view of the dual plenum shows the inlets to the mini oxidizer plenums. The downstream view of the dual plenum shows the injector exit surface. The dual plenum consists of the fuel plenum, 13 walled mini oxidizer plenums inside the fuel plenum section, and injector holes.

The engine is 135mm in length and 85 mm in diameter. The 13 mini oxidizer plenums have an internal diameter of 3 mm. They were critical for achieving the symmetric, square, lattice injector pattern in Figures 1 & 2: oxidizer travels from the oxidizer plenum, through the dual plenum via the mini oxidizer plenums, to the injector holes and into the combustion chamber below. The mini plenums are arranged in a diamond lattice pattern so injector holes could be arranged in the square lattice pattern. Since the square lattice injector pattern was used, to meet design guideline 1, the inside of the combustion chamber was also square (23 mm wide by 23 mm high to compare with [13], and 85 mm long) and uniformly spaced 1 mm from the injector holes. As for the injector holes, Figures 2 & 3 show 40 oxidizer holes of Ø0.6 mm and 40 fuel holes of Ø0.6 mm designed to create 40 impending jets and 40 mixing points. All the injector holes are placed at 45° angles from the injector exit face and injector holes are 2.2 mm apart. Pressure sensor holes are located on the combustion chamber on the top surface in the middle, and in the top corner, tangential to the wall, denoted as P_{Mi} and P_{Ci} respectively in Figure 4.

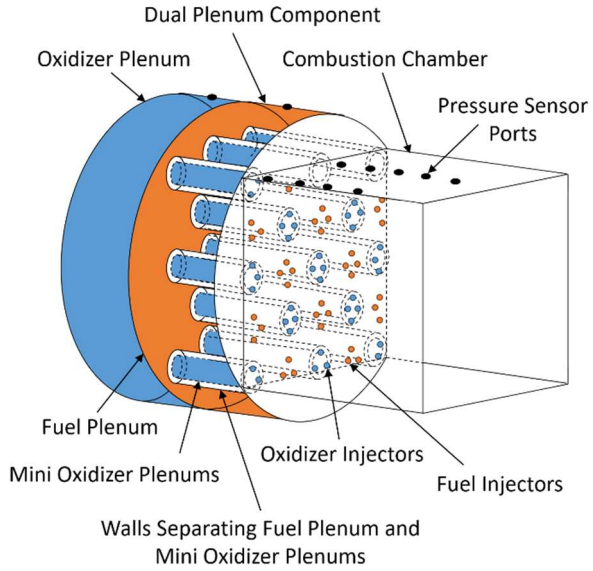

Figure 3: 3D Model of RDE Internal Structure

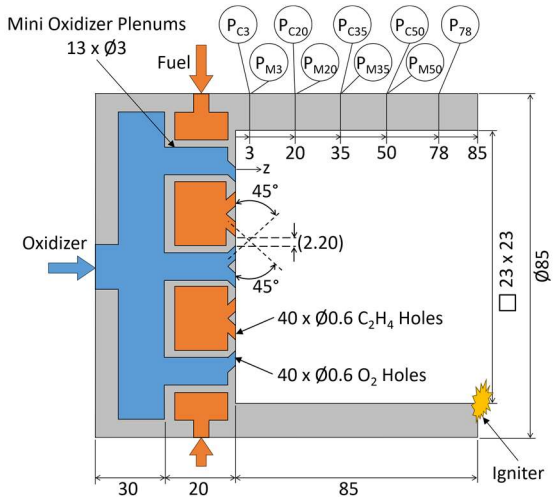

Figure 4 RDE Schematic with Dimensions (in mm).

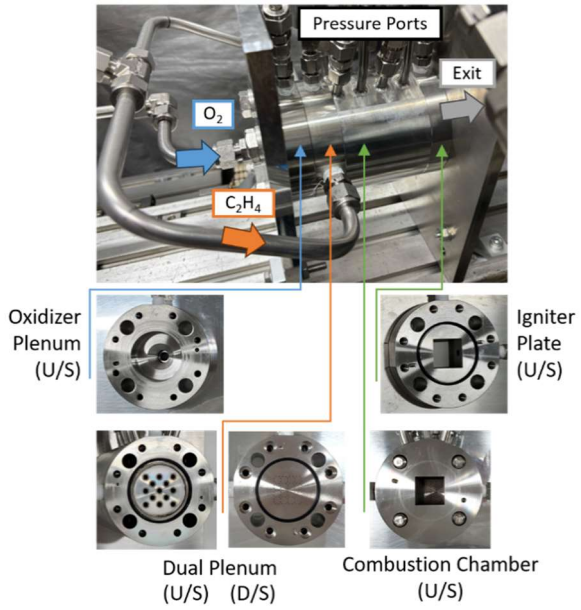

Figure 5: RDE Engine Assembly and Set Up

4. Experimental Set Up

The 30m^3 vacuum chamber at Nagoya University was used to conduct combustion experiments. The set up is depicted in Figure 6. Gaseous ethylene and gaseous oxygen were supplied from pressurized tanks, flowed through respective restricting orifices, past control valves, and into the engine. The engine was set up on a moving sled that pushed a load cell to measure thrust. High-speed and other cameras were set up to capture visual data from the engine exit. Pressure sensors installed on the engine according to Figure 4 captured pressure data from the combustion chamber.

The mass flowrate into the engine was controlled upstream of the engine by choking the orifices that supplied gases from the pressurized tanks. The load cell data from experiments was calibrated by comparing it to load cell measurements obtained under known loading. A Phantom v.2011 high-speed camera captured images showing wave propagation inside the combustion chamber. The Phantom camera settings were set to approximately 430,000 fps and 1.01 us of exposure for the Phantom. A SA5 FAST CAM and a Samsung Galaxy S10 captured footage of the engine plume (both used at various settings). Gunpower was attached at the engine exit and used to ignite the reactants.

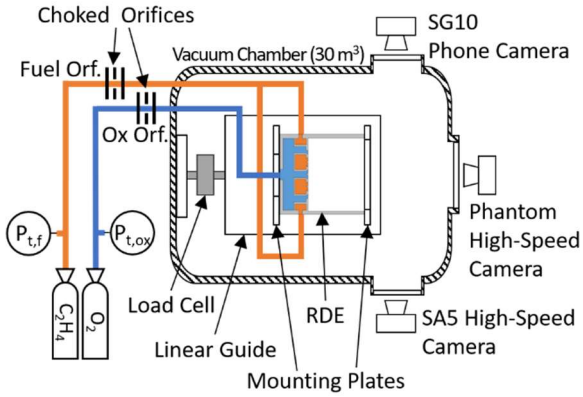

Figure 6: Test facilities experimental set up (top view).

5. Results and Discussion

Table 1 lists the experimental testing conditions. The total mass flowrate ranged between $\dot{m}_{tot}$ = 30 to 38 g/s, the equivalence ratio ranged between Φ= 1.0 to 1.6, and all combustion experiments were conducted from an initial back pressure of p_b=5 kPa. Engine performance parameters were calculated using time-averaged data from the combustion plateau (between t = 0.24 sec and 0.40 sec for shot 5 in Figure 7).

.

Table 1: Experimental Conditions and Results

Shot #	$\dot{m}_f$ [g/s]	$\dot{m}_{ox}$ [g/s]	$\dot{m}_{tot}$ [g/s]	ϕ [--]	p_{cc} [kPa]	p_{ex} [kPa]	p_b [kPa]	F [N]	I_{sp} [s]	D_w [m/s]	$\%D_{CJ}$ [%]	c* [m/s]
1	8.0	23.0	31.0	1.2	93.6	45.4	5	51.6	169	--[1]	--[1]	1300
2	7.6	22.8	30.4	1.1	92.5	46.7	5	50.5	169	2358	99	1305
3	7.9	27.0	35.0	1.0	89.7	48.8	5	51.9	151	--[1]	--[1]	1200
4	11.1	27.0	38.1	1.4	113.7	58.1	5	64.0	171	2358	99	1321
5	11.2	23.6	34.8	1.6	106	51.3	5	59.6	175	2224	94	1375
6	9.6	23.5	33.1	1.4	83.8	49.1	5	53.5	165	2310	97	1339

1Due to poor weather conditions, etc., it was not possible to acquire data to calculate this

The table values were calculated as follows: the mass flow rates of the reactants $\dot{m}_f$ and $\dot{m}_{ox}$were calculated using:

$$\dot{m}_{inj} = \frac{p_{ple}A_{inj}}{\sqrt{R_{gas}T_{room}}}\sqrt{\gamma\left(\frac{2}{\gamma+1}\right)^{\frac{\gamma+1}{\gamma-1}}}$$

From these, the total mass flowrate, $\dot{m}_{tot}$, and equivalence ratio, Φ, were calculated. The pressure in the combustion chamber, P_{cc} which is measured by P_{M3}, the pressure at the exit of the engine, P_{ex} which is measured by P_{78}, and the engine thrust, F, are calculated from the time-averaged combustion plateau data. The specific impulse, I_{sp}, is calculated according to:

$$I_{sp} = \frac{F_{avg}}{\dot{m}_{tot}g}$$

The wave velocity, D_w, is calculated using the footage captured by the Phantom high-speed camera (discussed below), D_{CJ} is calculated using NASA-CEA [14]. The characteristic velocity, c*, is calculated according to:

$$c^* = \frac{P_{cc}A_{cc}}{\dot{m}_{tot}}$$

These parameters are discussed below.

5.1 Pressure and Thrust Time Histories

Figure 7 shows the time history of the plenum pressure (a), thrust (b), pressure in the corner of the combustion chamber (c), and pressure at the middle surface of the combustion chamber (d) for shot 5 ($\dot{m}_{tot}$ = 34.8 g/s, Φ = 1.6, and p_b = 5 kPa).

In Figure 7, the ignition time is at t = 0 s. The time history graph shows that the pressure in the corner of the chamber is higher than the pressure in the middle of the chamber all along the combustion chamber length. This difference in pressure between the corner and the middle sensors is plotted in Figure 8. This difference generally reduces along the combustion chamber in all the tests. The only exception is at z = 35mm in shot 1 where instead, P_{M35} is greater than P_{C35} by 1.5%. This is

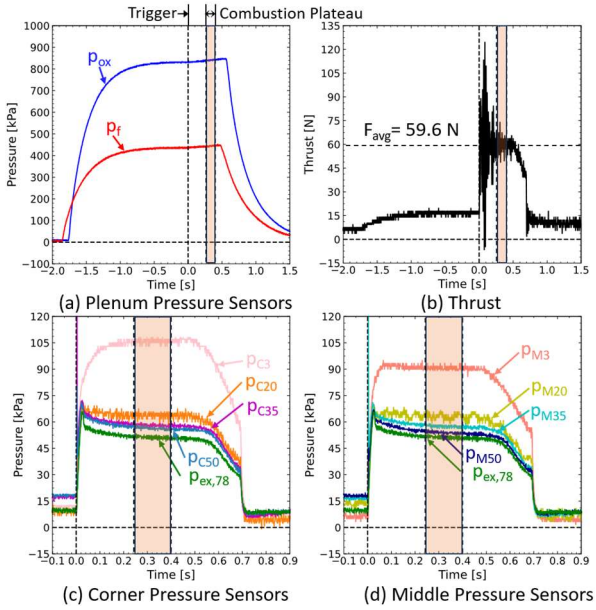

Figure 7: Pressure and Thrust Time History for Shot 5: m_{tot}= 34.8 g/s, Φ = 1.6, p_b = 5kPa.

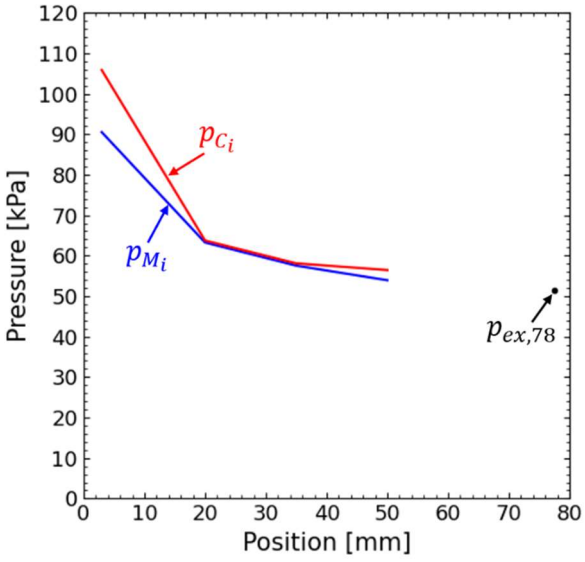

Figure 8: Pressure difference between corner and middle sensors along the combustion chamber for shot 5. m_{tot} = 34.8 g/s, Φ = 1.6, p_b = 5kPa.

potentially due to instrumentation error since all the other shots have $P_{C35} > P_{M35}$ at that location. On average, P_{Ci} is greater than P_{Mi} by approx. 20% at z = 3 mm, near the detonation wave front, 4% at z = 20 mm; 2.5% at z = 35 mm, and 5% at z = 50 mm. This increase in pressure at the corner may be due to the temporary shockwave that occurred when the detonation wave turned around the corner which is discussed next as well as other wave propagation phenomenon.

5.2 Propulsion Performance Parameters

The thrust and specific impulse obtained from this engine are around 70% of what was obtained from a hollow RDE tested at the university by [13]. However, the detonation wave velocity it 60% higher than that in [13], therefore there is some benefits to this symmetric, square lattice pattern injector RDE. The detonation wave velocity is discussed below. The characteristic velocity, on the other hand, is around 77% of the theoretical c* on average.

5.3 Wave Propagation Behavior

Along the walls, the detonation wave propagated without incident. While under stable operation, the detonation wave propagated in a single direction, either clockwise or counterclockwise for the entire combustion process. Only if a combustion instability occurred did the detonation wave change directions. This happened when the wave propagation mode changed to a reflective shuttling mode or deflagration mode temporarily near the end of a test. The reflective wave mode was identified as such by comparing the observed wave velocity and visual propagation manner to [15]. Combustion instabilities occurred in two of the six test cases, and after these instabilities the wave propagation direction changed.

In the corner regions, however, reflected shockwaves were observed (see Figure 9). The pressure time history plots in Figure 7 shows $P_{Ci} > P_{Mi}$. One contributing factor may be that when the detonation wave collided with the corner ahead of it, a temporary reflected shockwave occurred and increased the local flow pressure around P_{Ci}. However, this temporary shock wave dissipated before reaching the location of P_{Mi} causing P_{Mi} to be unaffected by it. As such, the local pressure of P_{Mi} would not be affected and result in $P_{Ci} > P_{Mi}$. The temporary shockwave observed may be similar to that which occurs in a shock tube when a shockwave hits the end wall and generates a reflected shock wave back into the shock tube.

Another possibly contributing factor is that when supersonic flow moves over a deflected wall, a shockwave is generated. This shockwave causes compression and also turns the flow around the deflection [16]. This may be what occurred as the detonation wave turned the corner in the square combustion chamber.

The large difference in P_{Ci} and P_{Mi} was observed at z=3 mm instead of at other downstream locations because z = 3 mm was likely closest to the z value where the detonation wave front traveled in the chamber [17].

5.4 Detonation Wave Velocity, D_w

A detonation wave velocity, D_w, has a maximum theoretical velocity: the Chapman-Jouget wave velocity, D_{CJ}. References [3] [6] are numerical studies showing that engine efficiency is impacted by D_w. Studies show lower velocity is due to non-ideal reactant mixing [5-7].

As mentioned, the detonation wave velocity was determined using images captured by the high-speed Phantom camera looking into the combustion chamber exit. Three random cycles for each shot were pictured, and the time used to complete one full rotation around the chamber was used.

Figure 10 shows the wave propagation for an arbitrary cycle of stable operation. The frames are positioned relative to the wave's location in the combustion chamber. The arrows from the frame to the central combustion chamber walls item show the wave's approximate location along the overall perimeter. The times around the chamber exit frame represent the time elapsed since the cycle began, and the velocities inside the center box are the wave velocity, the average velocity in the x direction, and the average velocity in the y direction. In Figure 10 specifically, D_w = 2333 m/s.

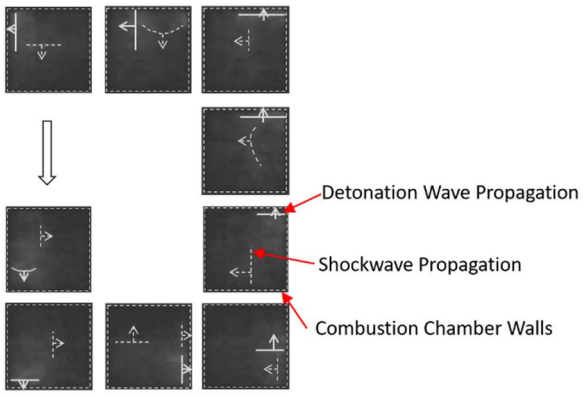

Figure 9: Reflected Shockwaves in the Combustion Chamber after Wave-Wall Collisions

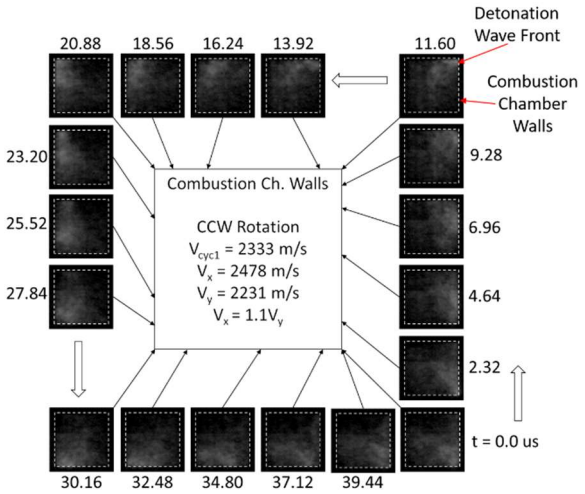

Figure 10: Detonation Wave Propagation in the Square Combustion Chamber and Associated Velocities for Shot 5, Random Cycle 1, m_{toto} = 34.8 g/s, Φ = 1.6, p_b = 5kPa.

The wave velocities obtained in shots 1-6 average 97% D_{CJ}. That is 17% increase over pintle injectors or crossflow jets (around 80% according to [10]) and an around of 46% higher than D_{CJ} obtained in previous experiments in a hollow, cylindrical RDE at Nagoya University [13]. The increase in wave velocity indicates using the symmetric, square, 2-dimensional, lattice pattern injector may have propellant improved mixing. Improved mixing may be due to various factors such as the 2-dimensional inflow across the entire injector exit surface area having impinging jets. Further visualization experiments could aid in identifying the source of the increased velocity.

Breaking the wave motion of the random cycle in Figure 10 into propagation along the horizontal x axis and vertical y axis, the random detonation wave cycle from shot 5 in shows a horizontal velocity of v_x = 2478 m/s, and V_y = 2231 m/s. Here, v_x is 10% larger than v_y. Eight of the 12 random cycles showed , $v_x \geq 1.1\ v_y$. The maximum observed percentage difference was v_x = 1.46 v_y (shot 6). One test case exhibited v_x = 0.8 v_y, and another exhibited v_x = 0.9 v_y.

6. Conclusion

In summary, this study found that to design a symmetric injector for a bi-propellant engine using a simple repeated shape, a square lattice pattern can be used. Expanding the square lattice pattern created a symmetric, two-dimensional injector flow field across the entire cross-sectional area, and that injector was then fitted with a square combustion chamber and tested.

The symmetric, square, two-dimensional, lattice pattern injector RDE was tested at mass flowrates between 30 – 38 g/s and equivalence ration between 1.0 – 1.6 at a back pressure of 5 kPa. The results showed an increased D_w of approximately 94% indicating this design may improve reactant mixing. Observations also showed unidirectional wave propagation under stable operation, and a reflected wave near the corners during stable detonation propagation increasing the corner pressure by 20% near the combustion chamber inlet.

Acknowledgements

The authors would like to thank NETS Co., Ltd. for their critical support and with whom this study was conducted as joint research. One of the authors (K. Higashino) is thankful to the Asian Office of Aerospace Research and Development for their partial support by the project number of FA2386-23-1-4061.

References

[1] Nordeen CA, Schwer D, Schauer F, Hoke J, Barber Th, Cetegen B. (2014). Thermodynamic model of a rotating detonation engine. Combust Explos Shock Waves. 50: 568.
[2] Zhou R, Wu D, Wang J. (2016). Progress of continuously rotating detonation engines. Chinese Journal of Aeronautics. 29: 15.
[3] Nordeen CA, Schwer D, Schauer F, Hoke J, Barber T, Cetegen BM. (2016). Role of inlet reactant mixedness on the thermodynamic performance of a rotating detonation engine. Shock Waves. 26: 417.
[4] Bigler BR, Bennewitz JW, Danczyky SA, Hargus Jr. WA. (2019). Injector Mixing Effects in Rotating Detonation Rocket Engines. AIAA 2019-3869.
[5] Sada T, Matsuo A, Shima E, Kawasaki A, Matsuoka K, Kasahara J. (2023). Numerical investigation of the effects of injector configuration on flow structures in annular and cylindrical rotating detonation combustors. Sci. and Tech. of Energetic Materials. 84: 17. (Online ISSN 2434-6322, Print ISSN 1347-9466).
[6] Anand V, Gutmark E. (2019). Rotating detonation combustors and their similarities to rocket instabilities. Progress in Energy and Combustion Science. 73: 183.
[7] Yi T-H, Lou J, Turangan C, Choi J-Y, Wolanski P. (2011). Propulsive Performance of a Continuously Rotating Detonation Engine. JPP. 27: 171.
[8] Duvall J, Chacon F, Harvey C, Gamba M. (2018) Study of the Effects of Various Injection Geometries on the Operation of a Rotating Detonation Engine. AIAA

2018-0631.
[9] Goto K, Yokoo R, Kawasaki A, Matsuoka K, Kasahara J, Matsuo A, Funaki I, Kawashima H. (2021). Investigation into the effective injector area of a rotating detonation engine with impact of backflow. Shock Waves. 31: 753.
[10] Goto K, Nishimura J, Kawasaki A, Matsuoka K, Kasahara J, Matsuo A, Funaki I, Nakata D, Uchiumi M, Higashino K. (2019). Propulsive Performance and Heating Environment of Rotating Detonation Engine with Various Nozzles. JPP 35:213
[11] Bykovskii FA, Zhdan SA, Vedernikov EF. (2006). Continuous Spin Detonations. JPP. 22: 1204.
[12] Kawalec M, Wolanski P, Perkowski W, Bilar A. (2023). Development of a Liquid-Propellant Rocket Powered by a Rotating Detonation Engine. Journal of Propulsion and Power. 39:554.
[13] Yokoo R, Goto K, Kim J, Kawasaki A, Matsuoka K, Kasahara J, Matsuo A, Funaki I. (2019). Propulsion Performance of Cylindrical Rotating Detonation Engine. AIAA Journal. 58: 5107.
[14] Gordon S, McBride BJ. (1996). Computer Program for Calculation of Complex Chemical Equilibrium Compositions and Applications. NASA Reference Publication 1311.
[15] Yamaguchi M, Taguchi T, Matsuoka K, Kawasaki A, Kasahara J, Watanabe H, Matsuo A. (2021). Investigation of combustion modes and pressure of reflective shuttling detonation combustor, Proceedings of the Combustion Institute. 38: 3615.
[16] Leipmann HW, Roshoko A. (2001). Elements of Gas Dynamics. New York: Dover Publications.
[17] Nakata K, Ishihara K, Goto K, Itouyama N, Watanabe H, Kawasaki A, Matsuoka K, Kasahara J, Matsuo A, Funaki I, Higashino K, Braun J, Meyer T, Paniagua G. (2023). Experimental investigation of inner flow of a throatless diverging rotating detonation engine. Proceedings of the Combustion Institute. 39:3073.